ARTICLES
https://doi.org/10.1038/s41561-018-0297-z
nature geoscience

Early and persistent supershear rupture of the 2018 magnitude 7.5 Palu earthquake

Han Bao[1], Jean-Paul Ampuero[2,3*], Lingsen Meng[1], Eric J. Fielding[4], Cunren Liang[3], Christopher W. D. Milliner[4], Tian Feng[1] and Hui Huang[1]

The speed at which an earthquake rupture propagates affects its energy balance and ground shaking impact. Dynamic models of supershear earthquakes, which are faster than the speed of shear waves, often start at subshear speed and later run faster than Eshelby's speed. Here we present robust evidence of an early and persistent supershear rupture at the sub-Eshelby speed of the 2018 magnitude 7.5 Palu, Indonesia, earthquake. Slowness-enhanced back-projection of teleseismic data provides a sharp image of the rupture process, along a path consistent with the surface rupture trace inferred by subpixel correlation of synthetic-aperture radar and satellite optical images. The rupture propagated at a sustained velocity of 4.1 km s^{-1} from its initiation to its end, despite large fault bends. The persistent supershear speed is further validated by seismological evidence of far-field Rayleigh Mach waves. The unusual features of this earthquake probe the connections between the rupture dynamics and fault structure. An early supershear transition could be promoted by fault roughness near the hypocentre. Steady rupture propagation at a speed unexpected in homogeneous media could result from the presence of a low-velocity damaged fault zone.

Although most earthquakes rupture at speeds lower than the shear wave velocity, faster, so-called supershear earthquakes have been predicted by theory and simulations[1,2] and observed in laboratory experiments[3] and large strike-slip earthquakes[4]. Whether observable fault properties control the occurrence of supershear rupture in nature is not completely understood. Supershear ruptures have been proposed to occur on smooth and straight faults[5], and to be promoted on fault segments with well-developed damage zones[6,7] and on geometrically rough faults[8].

On 28 September 2018, an earthquake with moment magnitude (M_w) 7.5 occurred in Sulawesi, Indonesia (Fig. 1). Its epicentre was located about 80 km north of the city of Palu. The earthquake ruptured along the Palu-Koro fault, a strike-slip left-lateral fault with a geodetic slip rate of 42 mm yr^{-1} (ref. [9]), a record of large earthquakes with magnitudes from 7 to 8 (ref. [10]) and previously identified seismic hazard[11]. This event triggered a tsunami and landslides that caused more than 2,000 casualties.

Here we focus on a feature of this earthquake that is important for our fundamental understanding of earthquake mechanics. We present robust seismological evidence of an early and persistent supershear rupture that propagates steadily at a speed that is thought to be unstable. We further exploit remote sensing observations of the rupture trace geometry to discuss possible relations between rupture speeds and fault structure.

Remote sensing observations of the surface rupture

Analysis of synthetic aperture radar (SAR) and optical images provides key constraints on the rupture geometry and the distribution of fault slip of the Palu earthquake. We measured the horizontal surface deformation due to the earthquake from a subpixel correlation of the interferometric synthetic-aperture radar and optical images (Methods). The SAR satellite tracks are very close to anti-parallel to the strike of the rupture, so the along-track displacements are almost parallel to the fault strike and show the location of the surface rupture on land where the east side moved north (positive in Fig. 1) and the west side moved south. Pixel tracking of the optical images provides a complementary data set that resolves the two-dimensional (2D) horizontal deformation pattern (Methods and Supplementary Fig. 10), where the north–south correlation maps shows a similar result to the SAR pixel offset.

Both data sets indicate that the inferred surface rupture has major geometrical complexities and differences between the northern and southern portions (Fig. 1a and Supplementary Fig. 1). No surface rupture was discerned north of the epicentre. The southern end of the surface rupture is at 119.99° E, 1.47° S (label E on Fig. 1a). The northern part of the rupture, from the epicentre to its intersection with the Palu Bay coast at 119.83° E, 0.69° S (label B), is less straight than the rupture from Palu city to the south. There is a substantial right bend on the rupture at 119.83° E, 0.34° S (label A on Fig. 1a), over which the fault trace is offset by about 4 km in the direction perpendicular to the main rupture strike. The rupture from Palu city (label C) to the south is very straight until it makes a large left bend at 119.885° E, 1.185° S (label D on Fig. 1a). The left bend is about 8.5 km along the diagonal and 6.5 km perpendicular to the main fault strike. The northern right bend and southern left bend are restraining and releasing, respectively, for the left-lateral Palu earthquake. The slip distribution measured from the optical image correlation maps (Methods) reveals the variation of fault slip along the surface rupture. The slip profile shows a maximum slip of 6 ± 0.5 m located near the city of Palu, and a clear difference in slip magnitude between the northern and southern segments, with an average slip of 1.9 m and 4.7 m, respectively (Fig. 1b).

Teleseismic back-projection supershear rupture imaging

A fast rupture during the Palu earthquake was first suggested by a large ratio between rupture length (estimated from the distribution of aftershocks and from satellite images) and the rupture duration inferred from teleseismic source time functions. Teleseismic

[1]Earth, Planetary and Space Sciences, University of California, Los Angeles, CA, USA. [2]Université Côte d'Azur, IRD, CNRS, Observatoire de la Côte d'Azur, Géoazur, France. [3]California Institute of Technology, Seismological Laboratory, Pasadena, CA, USA. [4]Jet Propulsion Laboratory, California Institute of Technology, Pasadena, CA, USA. *e-mail: ampuero@geoazur.unice.fr

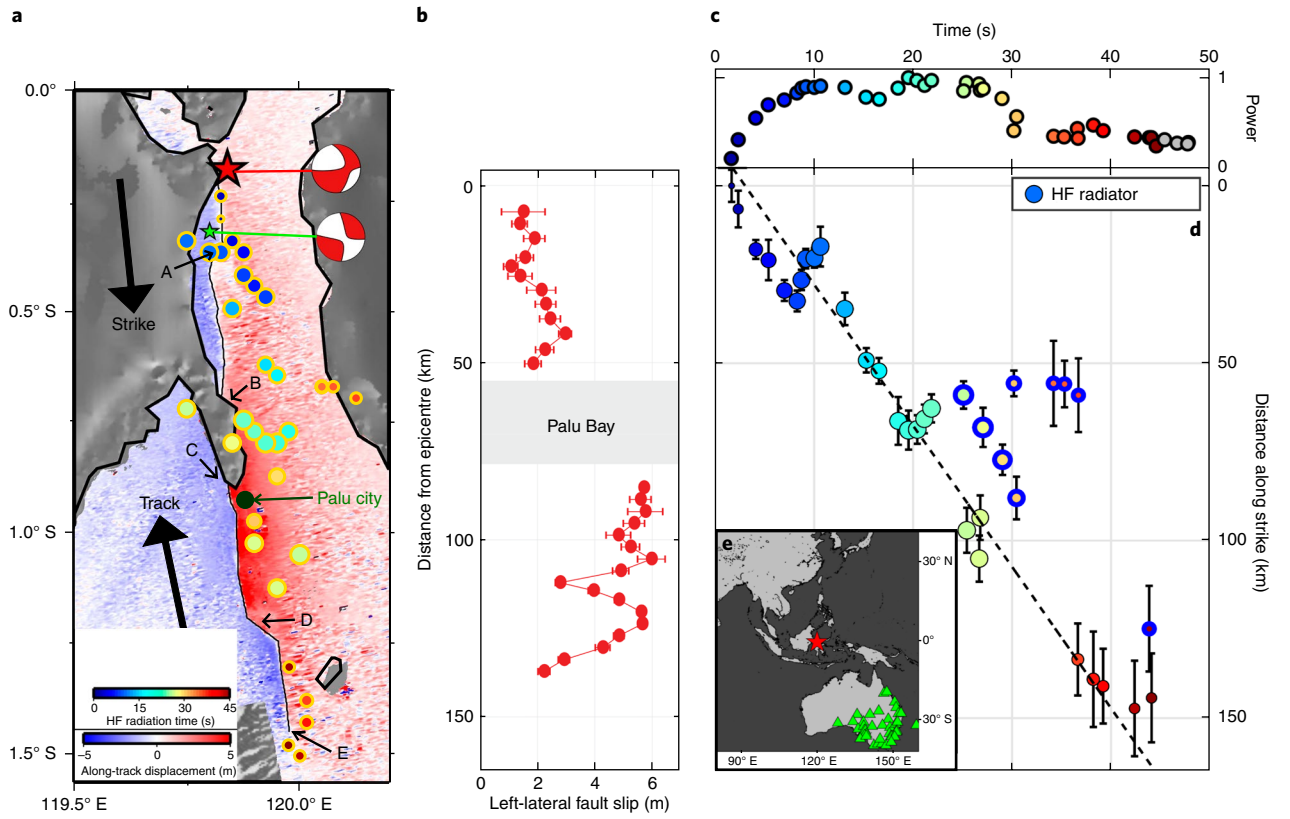

Fig. 1 | Surface rupture trace and supershear speed of the Palu earthquake. a, Along-track displacements from ALOS-2 SAR offsets (coloured image on land) and bathymetry (grey background offshore). The arrow labelled as 'Track' indicates the direction of measurement, -11.7°. The red star denotes the NEIC epicentre of the Palu earthquake. The green star is the relocated epicentre of the 28 September 2018 *M* 6.1 foreshock. The mainshock and foreshock focal mechanisms are also shown. The inferred surface rupture trace is indicated by a thin black line. Circles are the high-frequency (0.5–2 Hz) radiators imaged by the SEBP on data recorded by the Australia array, with size proportional to the relative energy and colour that represents the rupture time with respect to the mainshock origin time. **b,** Left-lateral slip distribution along the surface rupture measured from optical image correlation of the Sentinel-2 and Planet Labs data (Supplementary Fig. 10 gives the correlation maps). Fault slip is almost a factor of two larger on the southern segment through Palu city than north of the bay. **c**, Beam power as a function of time. Low-amplitude radiators after 45 s (grey) were not used in further analysis. **d**, Along-strike location and timing of radiators imaged by SEBP. Time is relative to the rupture origin time. Location is the horizontal position relative to the hypocentre, projected along the average strike direction (174°). The dashed line is a linear regression of the radiators close to the leading rupture front (circles with a blue rim are ignored). Error bars are location uncertainties derived from the slowness correction (Supplementary Fig. 11). **e**, The map shows the mainshock epicentre (red star) and stations of the Australia array used for SEBP (green triangles).

source inversion properly constrains the rupture duration but suffers from a strong trade-off between rupture size and rupture speed. Owing to the advent of regional dense seismic arrays, teleseismic back-projection rupture imaging has become one of the essential techniques to constrain the kinematic rupture properties of large earthquakes, such as rupture lengths, directions, speeds and segmentation[12]. Without prior knowledge of the fault geometry or the rupture speed, back-projection determines the location, timing and relative power of coherent high-frequency sources by exploiting the coherency of seismic waveforms across dense arrays. Here we apply the slowness-enhanced back-projection (SEBP) introduced by Meng et al.[13], a combination of the high-resolution MUSIC-multitaper back-projection method[14,15] and aftershock-based calibration of the slowness bias to mitigate the effects of the velocity structure heterogeneity (Methods).

The spatiotemporal characteristics of the kinematic rupture process are well imaged by SEBP of the recordings of the Australian seismic network (Fig. 1e). The slowness calibration systematically shifts the back-projection locations towards the south-southeast direction and reveals a longer, and thus faster, rupture than that imaged without calibration (Fig. 2). The accuracy of the calibration is supported by the agreement between the rupture lengths determined by SEBP and by remote sensing. Coherent sources with significant beam power occur until approximately 45 s after the rupture initiation (Fig. 1c). This source duration is consistent with the half-duration of 22.5 s reported by the routine United States Geological Survey (USGS) W-phase analysis (as in Data availability). The high-frequency sources follow an overall linear rupture path towards South-South-East, consistent with the surface fault traces identified by our SAR analysis (Fig. 1a). In two separate occasions, at around 10 s and 25 s, we observe more dispersed radiators, which suggests higher rupture complexities (Fig. 1a). The first episode of rupture perturbation coincides with the fault bend identified in the northern part of the rupture. The second episode roughly corresponds to the location of the Palu Bay, where the surface fault geometry is offshore and not visible on satellite images. The southernmost part of the rupture, south of the large left bend, has much smaller amplitude radiators (Fig. 1a).

Our SEBP reveals that the Palu earthquake rupture was supershear. We estimated the rupture velocity based on least-squares linear regression between the timing and the along-strike distance from the hypocentre of back-projection radiators in the first 45 s. We ignored the radiators that are not part of the leading rupture front (Fig. 1d). The radiators behind the leading front probably result from interference with the coda waves of earlier sources.

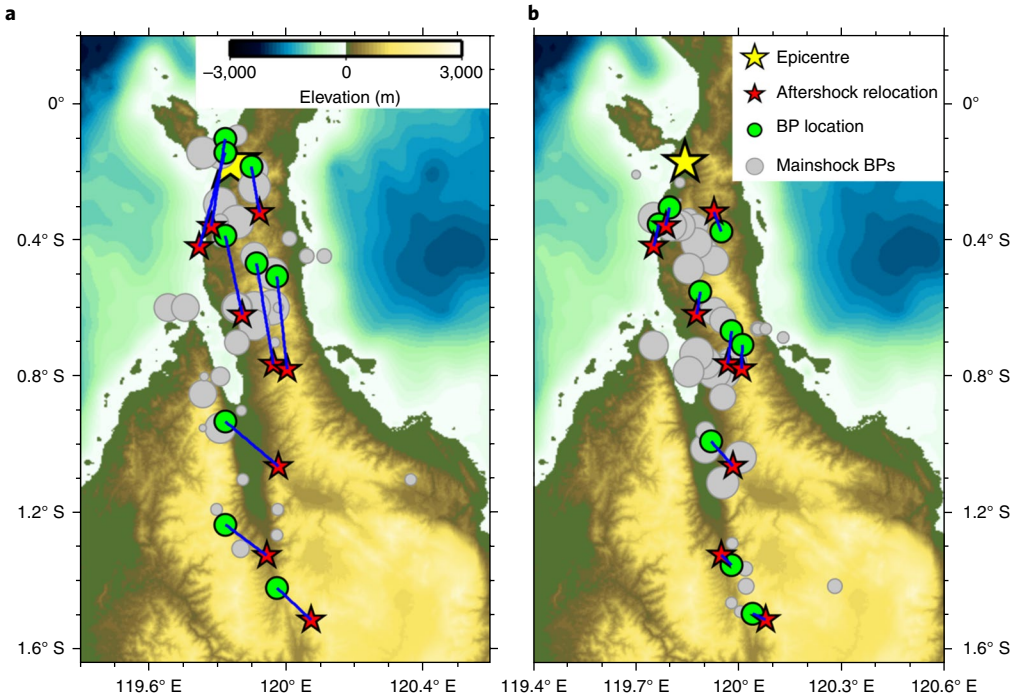

Fig. 2 | Calibration of back-projection based on aftershock data. a,**b**, Back-projection (BP)-inferred (green circles) and relocated (red stars) locations of nine *M* 5.0+ aftershocks that span the rupture region, and back-projection radiators (grey circles) before (**a**) and after (**b**) the slowness calibration. The results shown are for the Australia array.

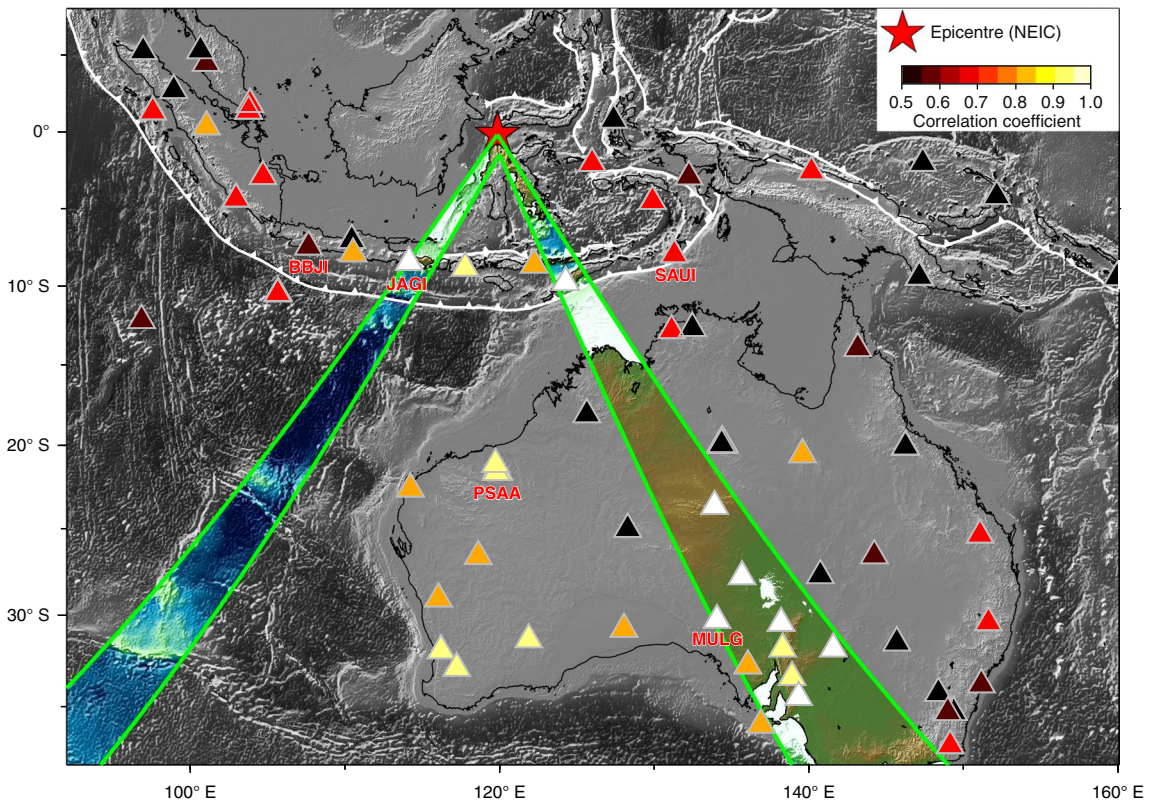

Fig. 3 | Evidence of a far-field Rayleigh-wave Mach cone. The coloured area within the green lines is the predicted area scanned by the Mach cone with the maximum possible Mach angle, based on the observed rupture velocity (4.1 km s^{-1}) and considering the uncertainty of Rayleigh wave phase velocity. The locations of the broadband stations are indicated by triangles. Their colour indicates the correlation coefficients between 15 to 25 s Rayleigh wave displacement seismograms of the Palu earthquake and its *M* 6.1 foreshock. Rayleigh waves recorded by the five stations with labelled names are shown in Fig. 4.

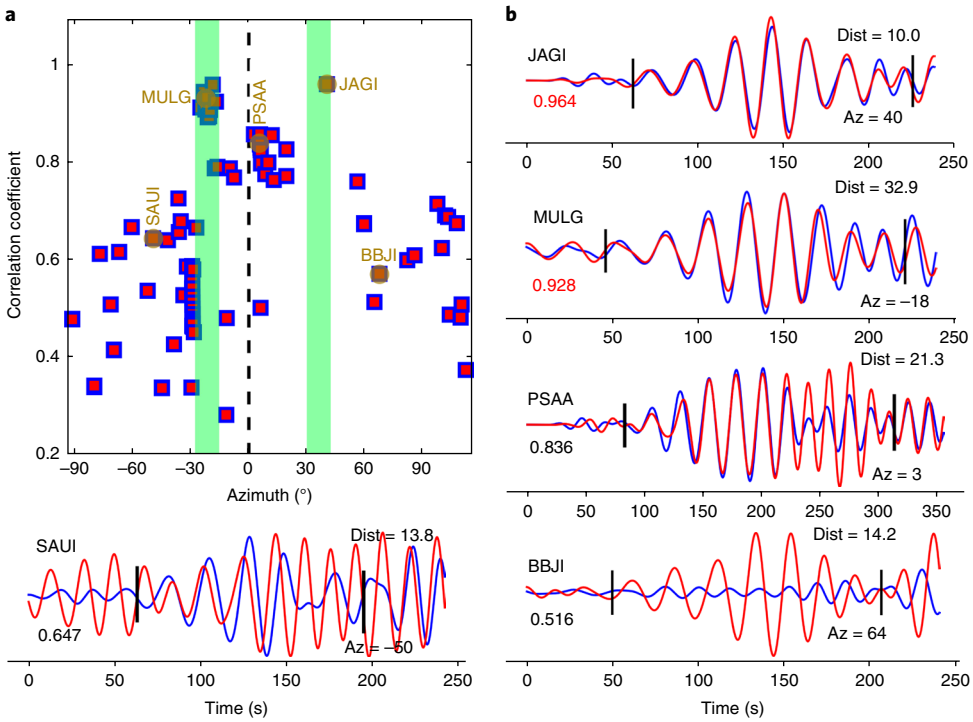

Fig. 4 | Evidence of Rayleigh Mach waves. a, Correlation coefficients (red squares) between 15 to 25 s Rayleigh waves of the mainshock and its *M* 6.1 foreshock (Fig. 1a) as a function of the station azimuth relative to the rupture strike. The dashed line indicates the fault strike direction. The two green bands indicate the estimated azimuth ranges of the two Mach cones, given uncertainties in the Rayleigh wave phase velocity and rupture velocity. The correlation coefficients reach the highest values at stations on the predicted Mach cone. **b**, Rayleigh wave vertical displacement seismograms of mainshock (blue) and foreshock (red) in the 15–25 s period range. Station name, azimuth (Az) relative to the rupture direction and hypocentral distance (Dist) are shown for each station. Values of the normalized cross-correlation coefficients, based on the signal windows between the two vertical ticks, are shown in red for stations on the Mach cones. Foreshock signals are scaled by the mainshock/foreshock moment ratio, 125.

The average rupture speed estimate and its s.d. are $4.10 \pm 0.15\,\mathrm{km\,s^{-1}}$ (Supplementary Information). The local shear-wave velocity in the Crust 1.0 model[16] ranges from 3.4 to 3.8 km s^{-1} at depths between 3 and 20 km, which cover the centroid depth of 13.5 km reported in the USGS W-phase solution and the typical depth range of the large slip in continental strike-slip earthquakes[17,18]. The rupture speed falls between the local shear-wave speed and the so-called Eshelby speed ($\sqrt{2}V_s = 4.8$~$5.3\,\mathrm{km\,s^{-1}}$). The supershear speed was sustained throughout the whole rupture, from the rupture onset to the end, as evidenced by the notable alignment of the radiators at the leading front in Fig. 1d. Remarkably, supershear rupture persists despite the major bends of the surface rupture. Our back-projection analysis does not show a resolvable initial sub-shear rupture phase observed in other supershear earthquakes[19–21].

Validation of supershear rupture

The supershear rupture speed indicated by our SEBP analysis is further validated by regional surface wave observations, given the absence of local strong motion data to search for a near-field signature of an S-Mach wave. The method was introduced by Vallée and Dunham[22] based on theoretical results by Dunham and Bhat[23] and exploits the rupture directivity effect (Methods). For regular sub-Rayleigh earthquakes, waves from different parts of the rupture arrive at a far-field receiver at different times. For supershear earthquakes this is also the case outside the Mach cone, but on the Mach cone waves from different parts of the rupture arrive simultaneously. Along the Rayleigh wave Mach cone, but not elsewhere, the waveforms of a large supershear rupture should be identical to those of a smaller collocated event with a similar focal mechanism, at periods shorter than the rupture duration of the supershear event and longer than its rise time. Their amplitude ratio should equal their seismic moment ratio. Such waveform similarities were first observed for the 2001 Kokoxili earthquake by Vallée and Dunham[22].

We inspected the Rayleigh wave resemblance between the Palu mainshock and a smaller M_w 6.1 foreshock recorded by regional broadband stations near Indonesia and Australia. The smaller event is located 30 km south of the mainshock hypocentre and has a similar focal mechanism (Fig. 1a). We filtered the Rayleigh waves in a narrow frequency band between 15 and 25 s to minimize the dispersion effect. We considered stations at epicentral distances up to 45° (Fig. 3). In such a large region, the Rayleigh wave phase velocity c is heterogeneous. Taking into account the space- and frequency-dependent variability of the phase velocity computed from the GDM52 model[24], we estimate $\bar{c} = 3.30 \pm 0.1$ km s^{-1} for the southwest side of the Palu earthquake and $\bar{c} = 3.75 \pm 0.1$ km s^{-1} for the southeast side. Based on the rupture velocity v_r resolved by SEBP, the angle between the far-field Rayleigh Mach cone and the rupture propagation direction is predicted as $\phi_M = \arccos(\bar{c}/v_r)$ (ref. [22]) (Fig. 3). Nine stations are located on the eastern Rayleigh Mach cone, whereas only one is on the western cone due to the poor station coverage over the Indian Ocean.

Waveforms from the mainshock and the foreshock are highly similar (correlation coefficients higher than 0.9) at the stations on the predicted Rayleigh Mach cone, but not at other azimuths (Figs. 3 and 4 and Supplementary Figs. 5–7). The amplitude ratios on the Mach cone are equal to the theoretically expected value given by the moment ratio between the two events, which is equal to 125. Stations located inside the Mach cone, including those located in the rupture direction, have smaller but still considerable similarities due to the directivity effect, whereas stations located outside the

Mach cone are the least similar. These results are consistent with the theoretical expectations (Methods) and provide immediate evidence that the supershear speed was persistent from the beginning to the end of the mainshock rupture, with a rupture velocity close to 4.1 km s^{-1}, which confirms our SEBP inferences.

Structural controls on earthquake rupture speed

The Palu earthquake rupture was supershear from very early on. In theoretical models and laboratory experiments, the transition to supershear triggered by the daughter-crack mechanism occurs at a certain rupture propagation distance[2,25,26]. In that context, a short transition distance implies a high initial shear stress on the fault or a short critical slip-weakening distance. Early supershear can also be triggered by the initial stress concentrations[26], which here could be due to the *M* 6.1 foreshock or to fault roughness. Bouchon et al.[5] noted that supershear ruptures happen on smooth faults, but in the Palu earthquake only the southern part of the surface rupture had a relatively simple geometry. A non-unique interpretation is that the smaller slip in the north is also indicative of the stronger fault roughness there[27]. Fault roughness in the epicentral area could have promoted the occurrence of a short-lived supershear episode, as found in dynamic rupture models[8], which then persisted over longer distances as the rupture continued on smoother sections of the fault, despite large-scale fault bends. Alternatively, the fault could be smoother at depth than at the surface.

Yet the supershear Palu earthquake rupture was not as fast as P waves. It was even slower than the Eshelby speed, which is at the lower end of stable supershear speeds in dynamic rupture models[28,29]. Steady rupture at a nominally unstable supershear speed can result from interactions between the dynamic rupture and head waves in a low-velocity damaged fault zone[6]. In that context, the Palu earthquake could be a stable supershear rupture that propagated at the P wave speed of a fault damage zone with a 30% reduction of wave speed relative to the host rock. Such a level of rock damage is not uncommon in mature fault zones[21]. The Palu-Koro fault has an accumulated slip larger than 100 km, large enough to have developed a mature damage zone. Pre-existing damaged fault zones also tend to shorten the supershear transition distance[6], which could also explain the early onset of supershear rupture in the Palu earthquake, but coseismic off-fault damage and dissipation may either accelerate[30] or delay[31] the supershear transition.

Supershear ruptures have the potential to generate strong ground shaking carried by Mach wave fronts, but the severity of this effect depends on the rupture speed[23]. In particular, a rupture running at the Eshelby speed does not produce a near-field S-wave Mach cone. To establish relations between the earthquake rupture speed and structural fault properties that can be mapped in advance is thus important to anticipate the impact of future earthquakes[7]. Further scrutiny is also warranted to determine if supershear rupture aggravated the impact of the Palu earthquake, including direct damage as well as liquefaction, landslides and their possible effect on the tsunami.

Online content

Any methods, additional references, Nature Research reporting summaries, source data, statements of data availability and associated accession codes are available at https://doi.org/10.1038/s41561-018-0297-z.

Received: 9 November 2018; Accepted: 21 December 2018;
Published online: 4 February 2019

References

1. Burridge, R. Admissible speeds for plane-strain self-similar shear cracks with friction but lacking cohesion. *Geophys. J. R. Astronom. Soc.* **35**, 439–455 (1973).
2. Andrews, D. J. Rupture velocity of plane strain shear cracks. *J. Geophys. Res.* **81**, 5679–5687 (1976).
3. Xia, K., Rosakis, A. J. & Kanamori, H. Laboratory earthquakes: the sub-Rayleigh-to-supershear rupture transition. *Science* **303**, 1859–1861 (2004).
4. Das, S. in *Perspectives on European Earthquake Engineering and Seismology* Vol. 2 (ed. Ansall, A.) 1–20 (Springer, Cham, 2015).
5. Bouchon, M. et al. Faulting characteristics of supershear earthquakes. *Tectonophysics* **493**, 244–253 (2010).
6. Huang, Y., Ampuero, J. P. & Helmberger, D. V. The potential for supershear earthquakes in damaged fault zones—theory and observations. *Earth Planet. Sci. Lett.* **433**, 109–115 (2016).
7. Perrin, C., Manighetti, I., Ampuero, J. P., Cappa, F. & Gaudemer, Y. Location of largest earthquake slip and fast rupture controlled by along-strike change in fault structural maturity due to fault growth. *J. Geophys. Res. Solid Earth* **121**, 3666–3685 (2016).
8. Bruhat, L., Fang, Z. & Dunham, E. M. Rupture complexity and the supershear transition on rough faults. *J. Geophys. Res. Solid Earth* **121**, 210–224 (2016).
9. Socquet, A. et al. India and Sunda plates motion and deformation along their boundary in Myanmar determined by GPS. *J. Geophys. Res. Solid Earth* **111**, B05406 (2006).
10. Watkinson, I. M. & Hall, R. in *Geohazards in Indonesia: Earth Science for Disaster Risk Reduction* (eds Cummins, P. R. & Meilano, I.) 71–120 (Geological Society Special Publications Vol. 441, Geological Society, London, 2017).
11. Cipta, A et al. in *Geohazards in Indonesia: Earth Science for Disaster Risk Reduction* (eds Cummins, P. R. & Meilano, I.) 133–152 (Geological Society Special Publications Vol. 441, Geological Society, London, 2017).
12. Kiser, E. & Ishii, M. Back-projection imaging of earthquakes. *Annu. Rev. Earth Planet. Sci.* **45**, 271–299 (2017).
13. Meng, L., Zhang, A. & Yagi, Y. Improving back projection imaging with a novel physics-based aftershock calibration approach: A case study of the 2015 Gorkha earthquake. *Geophys. Res. Lett.* **43**, 628–636 (2016).
14. Meng, L., Inbal, A. & Ampuero, J. P. A window into the complexity of the dynamic rupture of the 2011 M_w 9 Tohoku-Oki earthquake. *Geophys. Res. Lett.* **38**, L00G07 (2011).
15. Meng, L. et al. Earthquake in a maze: compressional rupture branching during the 2012 M_w 8.6 Sumatra earthquake. *Science* **337**, 724–726 (2012).
16. Laske, G., Masters, G., Ma, Z. & Pasyanos, M. Update on CRUST1. 0—a 1-degree global model of Earth's crust. *Geophys. Res. Abstr.* **15**, 2658 (2013).
17. Fialko, Y., Sandwell, D., Simons, M. & Rosen, P. Three-dimensional deformation caused by the Bam, Iran, earthquake and the origin of shallow slip deficit. *Nature* **435**, 295–299 (2005).
18. Xu, X. et al. Refining the shallow slip deficit. *Geophys. J. Int.* **204**, 1867–1886 (2016).
19. Vallée, M., Landès, M., Shapiro, N. M. & Klinger, Y. The 14 November 2001 Kokoxili (Tibet) earthquake: high-frequency seismic radiation originating from the transitions between sub-Rayleigh and supershear rupture velocity regimes. *J. Geophys. Res. Solid Earth* **113**, B07305 (2008).
20. Wang, D., Mori, J. & Koketsu, K. Fast rupture propagation for large strike-slip earthquakes. *Earth. Planet. Sci. Lett.* **440**, 115–126 (2016).
21. Huang, Y., Ampuero, J. P. & Helmberger, D. V. Earthquake ruptures modulated by waves in damaged fault zones. *J. Geophys. Res. Solid Earth* **119**, 3133–3154 (2014).
22. Vallée, M. & Dunham, E. M. Observation of far-field Mach waves generated by the 2001 Kokoxili supershear earthquake. *Geophys. Res. Lett* **39**, L05311 (2012).
23. Dunham, E. M. & Bhat, H. S. Attenuation of radiated ground motion and stresses from three-dimensional supershear ruptures. *J. Geophys. Res. Solid Earth* **113**, B08319 (2008).
24. Ekström, G. A global model of Love and Rayleigh surface wave dispersion and anisotropy, 25-250 s. *Geophys. J. Int.* **187**, 1668–1686 (2011).
25. Dunham, E. M. Conditions governing the occurrence of supershear ruptures under slip-weakening friction. *J. Geophys. Res. Solid Earth* **112**, B07302 (2007).
26. Liu, Y. & Lapusta, N. Transition of model II cracks from sub-Rayleigh to intersonic speeds in the presence of favorable heterogeneity. *J. Mech. Phys. Solids* **56**, 25–50 (2008).
27. Dieterich, J. H. & Smith, D. E. in *Mechanics, Structure and Evolution of Fault Zones* (eds Ben-Zion, Y. & Sammis, C.) 1799–1815 (Birkhäuser, Basel, 2009).
28. Burridge, R., Conn, G. & Freund, L. B. The stability of a rapid mode II shear crack with finite cohesive traction. *J. Geophys. Res.* **85**, 2210–2222 (1979).
29. Rosakis, A. J., Samudrala, O. & Coker, C. Cracks faster than the shear wave speed. *Science* **284**, 1337–1340 (1999).
30. Thomas, M. Y. & Bhat, H. S. Dynamic evolution of off-fault medium during an earthquake: a micromechanics based model. *Geophys. J. Int.* **214**, 1267–1280 (2018).
31. Gabriel, A. A., Ampuero, J. P., Dalguer, L. A. & Mai, P. M. Source properties of dynamic rupture pulses with off-fault plasticity. *J. Geophys. Res. Solid Earth* **118**, 4117–4126 (2013).

Acknowledgements

H.B. and L.M. were supported by NSF Earthscope grant no. EAR-1614609, NSF Geophysics grant no. EAR-1723192, and by the Leon and Joanne V.C. Knopoff Foundation. J.-P.A. acknowledges funding from the UCA-JEDI Investments in the Future project managed by the French National Research Agency (ANR, grant no.

ANR-15-IDEX-01) and from ANR grant no. ANR-17-CE31-0008-01. Part of this research was carried out at the Jet Propulsion Laboratory, California Institute of Technology, under a contract with the National Aeronautics and Space Administration (NASA) for the Earth Surface and Interior focus area and NISAR Science Team. The ALOS-2 original data are copyright JAXA and provided under JAXA ALOS RA6 PI projects P3278 and P3360. Sentinel-2 images used in our analysis contain modified Copernicus Sentinel data (2018), processed by the European Space Agency. We thank Planet Labs for access to their PlanetScope imagery. Funding for C.W.D.M. was provided under a NASA Postdoctoral Program fellowship administered by the Universities Space and Research Association through a contract with NASA. H.B. acknowledges that the Python software package ObSpy was used for data requesting, waveform filtering and cross-correlations.

Author contributions

J.-P.A. conceived and led the study. H.B. and L.M. performed the SEBP. H.B. performed the Rayleigh Mach wave analysis. C.L. and E.J.F. carried out the SAR image analysis. C.W.D.M. conducted the optical image analysis. J.-P.A., H.B., L.M., E.J.F. and C.W.D.M. wrote the paper and participated in the interpretation of the results. T.F. conducted a preliminary back-projection analysis. H.H. performed the aftershocks relocation.

Competing interests

The authors declare no competing interests.

Additional information

Supplementary information is available for this paper at https://doi.org/10.1038/s41561-018-0297-z.

Reprints and permissions information is available at www.nature.com/reprints.

Correspondence and requests for materials should be addressed to J.-P.A.

Publisher's note: Springer Nature remains neutral with regard to jurisdictional claims in published maps and institutional affiliations.

Methods

SAR analysis. To measure the net surface deformation due to the earthquake, we processed data from the Japan Aerospace Exploration Agency (JAXA) Advanced Land Observation Satellite-2 (ALOS-2) Phased-Array L-band Synthetic Aperture Radar-2 (PALSAR-2) instrument. We extracted along-track displacements in the ALOS-2 satellite track direction (azimuth −11.7° from north) using pixel offset tracking or subpixel image correlation[32] with the InSAR Scientific Computing Environment software[33]. We analysed PALSAR-2 images acquired in the fine-beam mode (approximately 4 m pixel spacing) on ascending paths 126 and 127 by precisely mosaicking the frames[34] before the pixel offset tracking using 128 × 128 pixel matching windows (Fig. 1). The data used are listed in Supplementary Table 1.

Optical analysis. To measure the 2D horizontal deformation pattern we used a subpixel correlation of the optical images acquired before and after the earthquake from the Sentinel-2 and Planet Labs sensors[35]. We used the image correlation method of Debella-Gilo and Kääb[36] applied to the visible bands. The method calculates the normalized cross-correlation between the images and achieves subpixel precision by interpolating for the correlation peak. To resolve the deformation field to the same scale given that the Sentinel-2 and Planet Labs imagery have different image resolutions (10 m and 3 m, respectively), we used correlation windows with step sizes of 9 and 30 pixels, respectively, which resulted in a consistent correlation map of 90 m pixel resolution (Supplementary Fig. 10). Areas of decorrelation in the result are caused primarily by clouds, which occur away from areas of the surface rupture and allow for the assessment of fault offset. We then measured the surface slip distribution (Fig. 1b) from the correlation maps using profiles perpendicular to the fault trace. We resolved the fault-parallel slip by projecting the surface displacement from the north–south and east–west displacement maps into the fault trace direction, and then estimated the slip magnitude from the offset between two linear trends that fitted either side of the fault[37]. The data used are listed in Supplementary Table 1.

Teleseismic SEBP. To achieve high-resolution rupture imaging, we applied the Multitaper-MUSIC array processing technique[14], which can resolve closer simultaneous sources and is less sensitive to aliasing than conventional back-projection techniques. The 'reference window' strategy[15] was also applied to eliminate the 'swimming artefact', a spurious migration of high-frequency energy towards the array due to the trade-off between the origin times of high-frequency sources and the source–receiver distances. To further reduce travel-time errors over the whole rupture, we applied the SEBP introduced by Meng et al.[13]. The conventional back-projection only requires knowledge of the hypocentre location and teleseismic travel times from the source region to the array stations. The latter are usually estimated assuming a 1D reference velocity model (for example, IASP91). The travel-time errors due to 3D path effects result in a 'spatial bias' of the subevent locations imaged by back-projection. A 'hypocentre correction' is routinely applied to mitigate travel-time errors[38,39]: travel-time corrections for the hypocentral region are estimated by cross-correlation of the initial P waveforms and then applied over the entire source region. However, the hypocentre correction is exact only in the immediate vicinity of the hypocentre and its effectiveness decreases in more distant parts of large ruptures[40,41]. The SEBP method accounts for the spatial derivatives of travel time in the source area through a slowness correction estimated from aftershock data. For a given aftershock, the differential travel time between its back-projection-inferred location and its hypocentre is compared to predictions based on the 1D reference model. The difference is mapped into the slowness correction term.

SEBP applied to the Australian network. We performed the SEBP on the high-frequency (0.5–2 Hz) P-wave seismograms recorded by 51 broadband stations of the Australian seismic network. Results based on other arrays are briefly summarized below. We first derived the slowness correction terms based on nine aftershocks with magnitudes that ranged from 5.0 to 6.1 and quite evenly distributed across the mainshock rupture zone (Fig. 2 and Supplementary Table 2). Their initial P waves have enough signal-to-noise ratio between 0.5 and 2 Hz at teleseismic distances. We relocated the aftershocks with respect to the mainshock hypocentre based on P-arrival times at regional stations, so that the locations are accurate enough for a reliable slowness calibration (Supplementary Table 2). The aftershock relocations are overall consistent with those reported by the National Earthquake Information Center (NEIC) and Geoforschungszentrum (Supplementary Fig. 2). Figure 2 compares the back-projection-imaged aftershock locations with and without the slowness correction. The initial back-projection locations (Fig. 2a) are generally biased northwestward with a root-mean-square error of 25.5 km. The bias is significantly reduced by our slowness calibration (Fig. 2b), down to a root-mean-square error of 7.6 km. Such a level of bias reduction is also demonstrated in back-projection studies of the 2015 M_w 7.8 Gorkha earthquake[13] and the M_w 8.3 Illapel earthquake[41]. We then applied SEBP to the mainshock data. The epicentre is assumed to be located at 119.840° E, 0.178° S, as reported by the NEIC. Due to the limited depth sensitivity of back-projection, we back-project at a fixed depth of 10 km (the NEIC hypocentre depth). Our confidence on the SEBP results comes from the remarkable agreement with the rupture path inferred from satellite images. Uncertainties in the hypocentre location can introduce a global spatial shift of the SEBP results. However, the difference between the epicentre locations issued by NEIC, Geoforschungszentrum (119.8800° E, 0.1800° S) and the Institut de Physique du Globe de Paris (119.8400° E, 0.1780° S) is less than 5 km, too small to affect the comparison to the satellite image analysis. Such an agreement was first achieved for the 2013 M_w 7.7 Balochistan earthquake[42]. Real-time automated back-projection has been proposed to complement earthquake and tsunami early warning[43,44] and rapid ground-motion estimations[45]. The slowness correction predetermined with background earthquakes is an important consideration for such applications.

SEBP applied to other teleseismic arrays. We also assessed the rupture imaging potential of four other regional arrays in Alaska, Japan, New Zealand and Turkey (Supplementary Fig. 3). The results based on the Japan and Alaska arrays are less satisfying due to the unfavourable interference between P and pP phases. The New Zealand array, in a similar azimuth as the Australian seismic network, gives results that are overall consistent with those of the Australian seismic network array but has a poorer resolution due to its smaller azimuthal aperture. For the Turkey array, our SEBP resolves a similar rupture length and an overall supershear speed (Supplementary Fig. 4).

Expected far-field surface wave similarity. The degree of waveform similarity between the large supershear rupture and a small event depends on the azimuth Φ between the rupture direction and the station. The expected dependence can be qualitatively explained by the directivity effect. This effect is well-known for body waves, and can be derived for surface waves from equations (3) and (4) of Vallée and Dunham[22]. The spectrum of the apparent source time function of a unilateral rupture is stretched or compressed by the directivity factor $D(\Phi) = 1 - \cos(\Phi)V_r/c$, which depends on the azimuth, rupture speed V_r and wave speed c (Supplementary Fig. 9). The spectral stretching is linear for body waves, and its time-domain counterpart is a compression of the source time function. However, for dispersive surface waves the spectral stretching is non-linear and does not induce a simple stretching in the time domain. The bandpass-filtered waveforms of a mainshock and a collocated foreshock are similar if their apparent source spectra are flat across the analysis frequency band. This happens if the apparent corner frequency of the mainshock, $1/(|D|T)$, where T is the rupture duration, is substantially higher than the dominant frequency $1/T_0$ of the filtered waveforms. In our analysis of the Palu earthquake, $T \approx 40$ s and $T_0 \approx 20$ s, and thus the condition for similarity is $|D(\Phi)| \ll 0.5$. Supplementary Fig. 9 shows in which azimuth ranges this condition is met, for various rupture speeds. We find that for sufficiently fast sub-Rayleigh ruptures, waveform similarity is maximal in the direction of rupture. For supershear ruptures, waveform similarity is maximal on the two Mach cones, but it can also be high in between if the rupture speed is sufficiently low.

Data availability

The ALOS-2 original data can be obtained from JAXA. Derived pixel offset maps can be obtained from the authors. Copernicus Sentinel images are available at no cost from the Copernicus Open Access Hub (https://scihub.copernicus.eu/). PlanetScope images are available from Planet Labs (https://www.planet.com/). The broadband seismograms are accessed from IRIS (www.iris.edu) data centres for the Australian and Alaskan networks, from ORFEUS (www.orfeus-eu.org) for the Turkish network, from GEONET (www.geonet.org.nz) for the New Zealand network and from Hi-net (http://www.hinet.bosai.go.jp) for the Japan network. The earthquake catalogues are obtained from the USGS NEIC (http://earthquake.usgs.gov). The background topography and bathymetry used in our figures are provided by the NOAA National Center for Environmental Information (https://www.ngdc.noaa.gov/mgg/global/etopo1sources.html). The USGS W-phase solution can be accessed at https://earthquake.usgs.gov/earthquakes/eventpage/us1000h3p4/moment-tensor. The computer code for back-projection is available upon request to L.M.

References

32. Pathier, E. et al. Displacement field and slip distribution of the 2005 Kashmir earthquake from SAR imagery. *Geophys. Res. Lett.* **33**, L20310 (2006).
33. Rosen, P. A., Gurrola, E., Sacco, G. F. & Zebker, H. in *EUSAR 2012: 9th European Conference on Synthetic Aperture Radar* 730–733 (IEEE, 2012).
34. Liang, C. & Fielding, E. J. Interferometry with ALOS-2 full-aperture ScanSAR data. *IEEE Trans. Geosci. Remote Sens.* **55**, 2739–2750 (2017).
35. Planet Team *Planet Application Program Interface: In Space for Life on Earth* (Planet, San Francisco, 2017).
36. Debella-Gilo, M. & Kääb, A. Sub-pixel precision image matching for measuring surface displacements on mass movements using normalized cross-correlation. *Remote Sens. Environ.* **115**, 130–142 (2011).
37. Leprince, S., Ayoub, F., Klinger, Y. & Avouac, J. P. in *Geoscience and Remote Sensing Symposium 2007* 1943–1946 (IEEE, 2007).

38. Ishii, M., Shearer, P. M., Houston, H. & Vidale, J. E. Extent, duration and speed of the 2004 Sumatra-Andaman earthquake imaged by the Hi-Net array. *Nature* **435**, 933–936 (2005).
39. Ishii, M., Shearer, P. M., Houston, H. & Vidale, J. E. Teleseismic P wave imaging of the 26 December 2004 Sumatra-Andaman and 28 March 2005 Sumatra earthquake ruptures using the Hi-net array. *J. Geophys. Res. Solid Earth* **112**, B11307 (2007).
40. Fan, W. & Shearer, P. M. Investigation of backprojection uncertainties with *M* 6 earthquakes. *J. Geophys. Res. Solid Earth* **122**, 7966–7986 (2017).
41. Meng, L. et al. Double pincer movement: encircling rupture splitting during the 2015 M_w 8.3 Illapel earthquake. *Earth Planet. Sci. Lett.* **495**, 164–173 (2018).
42. Avouac, J. P. et al. The 2013, M_w 7.7 Balochistan earthquake, energetic strike-slip reactivation of a thrust fault. *Earth Planet. Sci. Lett.* **391**, 128–134 (2014).
43. Meng, L., Allen, R. M. & Ampuero, J. P. Application of seismic array processing to earthquake early warning. *Bull. Seismol. Soc. Am.* **104**, 2553–2561 (2014).
44. An, C. & Meng, L. Application of array backprojection to tsunami prediction and early warning. *Geophys. Res. Lett.* **43**, 3677–3685 (2016).
45. Feng, T. & Meng, L. A high-frequency distance metric in ground-motion prediction equations based on seismic array back-projections. *Geophys. Res. Lett.* **45**, 11612–11621 (2018).